Estimation of flood inundation and depth during Hurricane Florence using Sentinel-1 and UAVSAR data

Sananda Kundu[1], Venkataraman Lakshmi[2] and Raymond Torres[1]

[1]School of Earth Ocean and the Environment, University of South Carolina, Columbia, SC, USA

[2]Department of Engineering Systems and Environment, University of Virginia, Charlottesville, VA 22904, USA

Corresponding author: Sananda Kundu (skundu@geol.sc.edu)

Key Points:

- Estimation of flood depth and changes in the water level during Hurricane Florence
- Observed data from USGS gauges are found to be well correlated with the estimated depths
- InSAR method gave better accuracy than the DEM and flood extent based method

Abstract

We studied the temporal and spatial changes in the flood water elevation and variation in the surface extent due to the flooding resulting from Hurricane Florence (September 2018) using the observation from an Unmanned Aerial Vehicle Synthetic Aperture Radar (UAVSAR) and Sentinel-1. The novelty of this study lies in the estimation of changes in the flood depth during the hurricane and investigating the best method. Overall, flood depths from SAR were observed to be well-correlated with the spatially distributed ground-based observations (R^2 = 0.79 to 0.96). The corresponding change in water level (h/ t) compared well between the remote sensing approach and the ground observations (R^2 = 0.90). This study highlights the potential use of SAR remote sensing for inundated landscapes (and locations with scarce ground observations), and it emphasizes the need for more frequent SAR observations during flood to provide spatially distributed and high temporal repeat observations of inundation.

Plain Language Summary

Hurricane induced flooding causes damages to property and the environment. It is important to assess the intensity of damage by estimating flood extent and depth. It is difficult to estimate the flood extent during the hazard in the forested and remote areas using in-situ observations, which makes it imperative to assess real time flooding using satellite data. We assessed the flood characteristics during Hurricane Florence in September 2018. Flood extent and depth was observed to be maximum on September 17 and 18, and gradually decreased till September 24. Flood depths were compared with the in-situ observations from gauges and the study emphasized the importance of using satellite data that can help to improve flood management and recovery efforts.

1 Introduction

Extensive flooding causes significant damage to infrastructure and limits access to natural resources (Kuenzer et al. 2013). Precise information on the flood extent can help property owners and government agencies to cope with the economic losses and for developing mitigation measures (Smith 1994). In order to provide essential information, it is necessary to assess the full extent of inundation, however, it is difficult to visualize a large flooded area due to several constraints (Martinis et al. 2009). Remote sensing using Synthetic Aperture Radar (SAR) is an effective method to monitor inundated areas. The major advantages are that it is independent of atmospheric conditions and can carry out mapping even under vegetated conditions (Woodhouse, 2017). Recently, natural disasters worldwide have shown that remote sensing technology can be used in different phases of disaster management such as preparedness, prevention, relief, and reconstruction (van Westen, 2000).

The return period of floods is estimated to decrease (Pall et al., 2011; Arnell and Gosling, 2016) and studies have already indicated an increase in the extreme precipitation (Min et al., 2011; Westra et al., 2013). However, there is limited global evidence regarding the trend in the magnitude of annual maximum floods and their prediction (Kundzewicz et al., 2014).

The majority of literature on the use of SAR has focused on flood inundation in forested areas and wetlands (Schlaffer et al., 2015; Twele et al., 2016; Pradhan et al., 2017; Chini et al., 2017; Amitrano et al., 2018). In addition, most of these studies focus solely on the areal extent of inundation (Huang and Jin, 2020; Zeng et al., 2020) and only a handful address changes in water level and dynamics of flood depth. Alsdorf et al., (2001; 2000) examined water level dynamics along parts of the Amazon floodplain using Shuttle Imaging Radar (SIR-C) L-band observations. They found that water level changes in the inundated vegetation can be measured using the L-band HH polarization observations. Brown et al. (2016) estimated the flood boundary from the SAR data and flood surface elevation using the digital terrain model derived from LiDAR data to obtain flood depth. Zhang et al. (2018) mapped the flood extent and change in the water level during Hurricane Irma using Sentinel-1 data and concluded that the majority of their study area in South Florida was impacted by flooding. However, some recent studies have used only SAR or integrated SAR and hydrological modeling for estimating flood inundation. Dasgupta et al. (2020) have compared SAR derived flood extent to the hydrodynamic modeling in Mahanadi. Psomiadis et al. (2019) estimated flood depth in Greece using Sentinel-1 and Digital Elevation Model (DEM). Grimaldi et al., 2020 have used SAR to map flood under vegetated cover while urban flood inundation and mapping was done by Bhatt et al. (2019) in Jammu and Kashmir of India using SAR observations. Urban flood such as the one in Houston in 2017 and Joso of Japan were studied by Li et al. (2019) using Sentinel-1 and ALOS-2 data and Houston flood caused by Hurricane Harvey was studied by integrated SAR and hydraulic modeling by Scotti et al. (2020). Hydraulic model was used here to estimate the flood depth

and velocity and compared with the SAR derived flood inundation. However, for large area flooding, hydraulic models may not be appropriate to estimate flood extent and depths. Recent studies on flood detection using SAR data are carried out by Wan et al. (2019); Wu et al. (2019), Sharifi (2020). Hultquist and Cervone (2020) have used SAR product for estimation, Wdowinski et al (2004) worked on wetland inundation, and Liang and Liu (2020) proposed a method to estimate daily inundation based on flood map information from multiple sources. However, in our study difficulties in estimating the hurricane flood was experienced even while using high quality data of UAVSAR and Sentinel-1. In this paper both Sentinel-1 and UAVSAR were used and results from both were presented so that it can be compared and best method with better accuracy can be indicated. All these studies have observed flood using SAR and integrating other methods or have used products, but very few have directly estimated and compared depth from different methods using DEM and interferometry for a major hurricane.

Most of the remote sensing studies use either L (1-2 GHz) or C (4-8 GHz) frequency to obtain changes in the water level. The L-band is better suited for identifying water in forested areas as compared to the C-band, however, for sparsely vegetated areas and in leaf-off conditions, C- or X-band (10 GHz) can also be used to map flooded vegetation (Lang et al., 2008; Voormansik et al. 2013; Martinis and Rieke 2015; Plank et al., 2017). Lu and Kwoun (2008) used European Remote Sensing (ERS)-1/ERS-2 with C-band and VV polarization and found that the Interferometric Synthetic Aperture Radar (InSAR) maintained sound coherence and could measure the changes in phase over the wet forest areas in Southeast Louisiana.

The main aim of the present study is to investigate and assess depths obtained by two different methods (DEM and InSAR) to provide the best result during hurricanes with a short duration, where water recedes quickly but results in extensive damages. Results and analysis of the study has the potential that can be followed to estimate extensive flood in case of other hurricanes or disaster induced floods, with comprehensive comparison against the observed USGS ground data. This analysis provides a significant direction to the techniques that can be best suited in hurricane flood depth estimates. To accomplish this, we estimated changes in the flood extent and water level in South Carolina during the passage of Hurricane Florence (September 2018) using two high resolution data - the C-band (5.405 GHz) Sentinel-1 and L-band (1.25 GHz) Unmanned Aerial Vehicle Synthetic Aperture Radar (UAVSAR) and compared the results with the USGS gauge data.

2 Materials and Methods

2.1 Study area

The Pee Dee River Basin covers about 18,702 km^2 in North and South Carolina, United States, and drains into the Atlantic Ocean via the Winyah Bay in South Carolina. The Black River, Waccamaw River, and Pee Dee River are considered

as the largest rivers within the Yadkin Pee Dee River Basin in South Carolina (Majidzadeh et al., 2017). Our study site is the Pee Dee River basin in South Carolina with a flooded area of 5,607 km^2 (Figure 1) on September 18, 22, and 23, 3,486 km^2 for the September 17 and 4,622 km^2 for September 24. The study sites were selected based on the availability of the UAVSAR flight lines and Sentinel-1 data during the passage of Hurricane Florence between September 17 to September 24, 2018. The Light Detection and Ranging (LiDAR) digital elevation model (DEM) was used in the Pee Dee River Basin area to obtain the flood depth. The elevation of the study site is around 132.85 m in the north. The extreme southeast of our study area has a low elevation near the coastline and it increases towards the north along both sides of the Pee Dee River. Observed data from the United States Geological Survey (USGS) gauge stations in the Pee Dee River Basin were used to compare with the computed flood depth from the DEM and the differences in the water level inferred from the interferogram obtained from SAR during the passage of Hurricane Florence.

2.2 Data

The UAVSAR and Sentinel-1 data were used in the study for estimation of flood extent, depth and changes in the water level. Observed data from the 9 USGS gauges located within the study area were used that recorded the gauge heights during Hurricane Florence (Table S1). The LiDAR DEM of 3 m spatial resolution of vertical datum of North American Vertical Datum (NAVD88) was used in the analyses. All the USGS gauges used here have NAVD88 datum (Table S1, S2, and S3).

Our flood estimates rely on two sets of SAR data - UAVSAR and Sentinel-1. UAVSAR is a Jet Propulsion Laboratory (JPL) based airborne pod-mounted polarimetric instrument that provides a repeat-pass interferometric observation system with a 16 km swath and operates at 1.26 GHz frequency and HH polarization. The UAVSAR used in this work has a fine spatial resolution (Table S2). The horizontal transmit and horizontal receive (HH) polarization of InSAR pair of Ground Range Detected (GRD) data of UAVSAR was used to identify the flooded area as it can penetrate the vegetation canopy and displays a good contrast between land and water (Brisco et al., 2008; 2009).

Sentinel-1 is a C-band system developed by European Space Agency with a 250 km Interferometric Wide Swath (IW). Sentinel-1 data were obtained from the Alaska SAR Facility (ASF) EarthData site. The Sentinel-1 data constellation consists of two satellites in the same orbital plane, Sentinel-1A, and Sentinel-1B (https://Sentinel.esa.int/web/Sentinel/missions/Sentinel-1/overview). The Sentinel-1 products are useful for flood mapping and monitoring due to its frequent revisit time (6 days for the constellation). The level-1 GRD and Single Look Complex (SLC) data from Sentinel-1A/B were used for September 18 and 24 of 2018 to estimate the difference in the level of flood water between the two dates. VV polarization (vertical transmit and vertical receive of waves by the antenna) was selected in this study since it is considered to have better accuracy than VH (Twele et al. 2016). Co-polarization such as VV has the

ability to detect partially submerged features, which is beneficial in flood damage assessments (Manjusree et al. 2012). However, HH polarization is preferred for estimating flood inundation because it is considered to be less sensitive to minor vertical differences due to waves on the water surface (Martinis et al., 2009, Gan et al., 2012). Therefore, VV and HH polarization were selected for this study.

2.3 Methodology

The remotely-sensed (UAVSAR and Sentinel) amplitude data were corrected and geo-referenced, and converted to backscatter values to identify the flooded and non-flooded areas (Manjusree et al., 2012; Liang and Liu, 2020). The permanent water bodies were identified from the Landsat 8 image during a non-flooded period (May 2018) using the Normalized Difference Water Index (NDWI) method (Chen et al., 2006). NDWI is related to the vegetation water content based on physical principles (Gao, 1996). Month of May was the dry month and hence water available during this time remains throughout the year as permanent water. The permanent water body extracted by this method was eliminated from the inundated areas to obtain the flooded areas. The threshold method was used to differentiate between flooded and non-flooded areas (Zhang et al., 2018) and permanent water features were used as a base reference for selecting flood thresholds. At the C-band VV polarization, the backscatter coefficient varies between -6 and -15 dB for water while in VH polarization it varies between -15 and -24 dB (Manjusree et al., 2012). In our study also, the threshold values in Sentinel-1 with VV polarization was within this given limit. Flooded area extraction using backscatter observations relies on threshold-based methodology, which requires to carefully identify the proper threshold backscatter value for water body detection (Manjusree et al., 2012; O'Grady et al., 2013). Interferometric processing was carried out using SLC data from Sentinel-1 (Alsdorf et al., 2000; Jung et al., 2010) to obtain a change in the water level (h/ t) (Zhang et al., 2018). Preprocessing of the Sentinel-1 data was carried out in VV polarization with IW mode and along with the UAVSAR data was used to estimate the extent of floodwater using the threshold method. Co-polarization like VV and HH are preferred for smooth surfaces like for flood over cross-polarization (Gan et al., 2012). Use of interferometry processing of L-band SAR data was demonstrated by Alsdorf et al. (2000) for the first time to detect changes in the wetland water level. Change in the water level is recorded between two acquisition dates that shows a change in phase of interferogram. We have followed the pre-processing instructions of the SAR data provided by the Sentinel Application Platform (SNAP) of the European Space Agency including speckle and terrain correction. Additional filtering was not done to retain the fine pixel resolution of the image. The ground range detected (GRD) product comprises information for converting digital pixel values into backscatter intensity. UAVSAR data are high precision aerial data processed and provided by the JPL lab. To retain the fineness of this data, no speckle correction was carried out on these images.

The LiDAR DEM was used to determine the flood depth on the different dates

using the extent of the flooded area. LiDAR data were obtained from the South Carolina Department of Natural Resources (SCDNR). The corresponding LiDAR DEM-based water depths were then compared against the USGS gauge data. Estimation of water depth on different flooded days was carried out by extracting the boundary cells of the flooded area and assigning their DEM elevations in the surrounding area by iteration (Cohen et al., 2018).

Our analyses use the LiDAR DEM and radar interferometry to estimate the depth and the difference in the water level between two dates. The water elevation changes measured from the interferogram along the direction of the radar line-of-sight (LOS) was converted to the vertical displacement with the wavelength and incidence angle (Jung et al., 2012).

3 Results

3.1 Water level during Florence and flood depth estimation

Variation in the gauge heights obtained from the 9 USGS gauges during Hurricane Florence is depicted in Figure S1. The X-axis indicates dates from September 14 to September 24, 2018. Few gauges have data starting from September 17 and gauge 2110802 (A) and 2130561 (F) have missing data. The gauge heights reach the highest level on September 17 and in some gauges the peak level was reached on September 20-21, following which there is a gradual decrease in heights to September 24. 3 gauges - gauge 2130980 (TA), gauge 2130561 (F), and gauge 02130000 (G) showed that the maximum height is reached on September 17 and one on September 18 (gauge 2130930 i.e. TB); 3 gauges - gauge 2131010 (C), gauge 2131000 (D), and gauge 2130810 (E) showed gradual increase to a maximum on September 20-21 and the remaining 2 gauges - gauge 2110802 (A) and gauge 2135200 (B) showed continuous increase up to September 24.

The spatial distribution of flood depths is shown in Figure 2, which was estimated using the flood extent and the LiDAR DEM. Depth estimation by this method indicated a range of depths from less than 0.5 m to greater than 4.5 m over the study area. About 7% of flooded area on September 17, 9% and 8.8% on September 18 in Sentinel-1 and UAVSAR respectively, 13.5% on September 22 in UAVSAR, 14% on September 23 in UAVSAR, and 15% in Sentinel-1 on September 24, 2018, showed the flooded depth of less than 1 m. Depth of floodwater was highest on September 17 and 18 and decreased gradually to September 24. However, errors in the estimation process were observed as negative values of depth, which imply no flood depth in the area. Negative values are observed in about 5% of the area on September 17, 2018, 7% of the area on September 18, 2018, decreasing to about 3% on September 24, 2018. Areas of high values of more than 15 m are estimated to vary from 0.09 to 0.65% of the flooded area. Underestimation of flood depth values is observed in most of the study area, which might be due to error caused by the location of the flood boundary cells on big water bodies (Cohen et al., 2018).

Table S4 shows the distribution of flood depth with respect to the total flooded

area for each day during Hurricane Florence computed from the flood extent and DEM. As observed from the data, September 17 and 18 of 2018 experienced maximum area (>4.5 m) under high flood water depth (4.64% on September 17, and 2.53% and 5.83% on September 18 for Sentinel-1 and UAVSAR respectively), and September 22 and 23 showed lowest percentage areas of maximum flood depth (0.14 and 0.12% respectively). From September 17 to 24, areas of low flood depth (<1 m) increased while areas of maximum flood depth (>4.5 m) decreased. The peak flood was observed on September 18 of 2018.

The water depths are obtained by differencing water surface elevation and land surface elevation (i.e., DEM), which were then compared with the observed data from USGS gauges (Figure 3A). The Pearson correlation (R^2) for all dates for this comparison varies from 0.79 on September 22 to the highest R^2 of 0.96 on September 18, 2018 (UAVSAR). For other dates we observe that R^2 varied between 0.86 to 0.95. The root mean square error (RMSE) varies from 1.69 m on September 17 to 13.59 m on September 24. The depths estimated from UAVSAR and Sentinel underestimated the observed depth from the USGS gauge data but for a few exceptions. We observe that the USGS gauge F (Pee Dee River near Bennettsville) displays overestimation for September 18, 22, and 23 of 2018 (UAVSAR) and slight overestimation was also observed in the USGS gauge of A (Waccamaw River at Bucksport) for September 17 and 18, 2018.

3.2 Estimation of the difference in water level using interferogram

The temporal variation of the water heights (h/ t) between September 18 and 24 of 2018 obtained from the USGS gauge data were compared with that obtained from the interferogram using the Sentinel-1 data (Figure 3B). The two dates of September 18, which corresponded to the peak flood, and September 24 corresponding to the lowest floodwater were used to show the changes in elevation of the water level. A correlation of 0.9 was observed between the USGS gauges and the h/ t of the interferogram. Sentinel-1 images do not cover the entire study area on September 24, therefore only the 6 USGS gauge stations within the available study area were used.

Comparison of errors of two methods in change of water level between two dates is illustrated in Figure 3C. 6 gauges are indicated here, where change of flood water level is negative in gauges D and E. Similar results are observed in the water level change obtained from the interferogram, but the change in water level obtained from DEM are positive. In gauge F, the change in water level is underestimated in DEM, while it is overestimated in interferogram in respect to the observed data. In gauge G, the interferogram underestimated the change more than the result obtained from DEM. In gauges TA and TB, change in level obtained from both the methods are overestimated, however overestimation is more in gauge TB by DEM than interferogram. Analysis of daily change in depth during hurricanes is very crucial. UAVSAR and Sentinel-1 data indicated change in the flood level with gradual recession in the entire hurricane duration.

However, the peak of the flood occurs on September 18 after the precipitation

declines - as observed from gauge heights of different gauge stations, precipitation was high between September 14 to 16, 2018 in the study area. The gauge height increases between September 17 and thereafter declines from September 21, 2018. A similar observation in Figure 3 implies a rise in the flood water to peak on September 18 and the study area remained submerged till September 22-24, 2018.

4 Conclusions

This study includes the combined approach of determination of flood depth and the difference in water level (h/ t) using Sentinel-1, UAVSAR, and LiDAR DEM. The analyses provide a noteworthy direction to the type of data and techniques used that would give precise result in estimating hurricane flood depth, and also for storms where water recedes quickly. Previous studies of inundation by radar remote sensing typically focused on flood mapping and do not include depth analysis that determines the intensity and damage from a major flood event induced by the hurricane. Use of modeling is time exhausting and is not always suitable for large areas. This study provides a breakthrough, firstly, by estimating daily changes in the flood depth, which is difficult to obtain due to absence of high quality daily SAR data, and secondly, we endeavored at highlighting the method that would be precise in hurricane flood depth estimation with short duration. We observed the maximum inundation with a higher range of depth (>2m) due to flooding on September 18 using Sentinel-1 and UAVSAR data. We also found good correlation in the water level variation - h/ t from USGS gauge height and that generated by interferometry. Interferometry indicated a comparatively better accuracy when compared with the gauge data. Therefore, short duration hurricane floods, which are difficult to assess can follow this using high quality data. This approach is particularly useful in locations with little or no ground observations as this can help to schedule relief operations and help in land use management.

Acknowledgments and Data

The financial support for this work was received from NASA (grant no. NASA SC EPSCoR award NNX16AR02A). The authors are thankful to the JPL, NASA for the UAVSAR data (https://uavsar.jpl.nasa.gov/cgi-bin/data.pl), and the European Space Agency (ESA) for the Sentinel-1 data (https://vertex.daac.asf.alaska.edu/#). The South Carolina Department of Natural Resources (SCDNR) (http://www.dnr.sc.gov/GIS/lidarstatus.html) provided the LiDAR DEM, and the United States Geological Survey (USGS) provided gauge data (https://waterdata.usgs.gov/sc/nwis/rt/) and Landsat data obtained from the Earthexplorer (https://earthexplorer.usgs.gov/).

References

Alsdorf, D. E., J. M. Melack, T. Dunne, L. A. Mertes, L. L. Hess, and L. C. Smith (2000), Interferometric radar measurements of water level changes on the Amazon flood plain, Nature, 404(6774), 174-177.

Alsdorf, D. E., L. C. Smith, and J. M. Melack (2001), Amazon floodplain water level changes measured with interferometric SIR-C radar, IEEE Transactions on Geoscience and Remote Sensing, 39(2), 423-431.

Amitrano, D., G. Di Martino, A. Iodice, D. Riccio, and G. Ruello (2018), Unsupervised rapid flood mapping using Sentinel-1 GRD SAR images, IEEE Transactions on Geoscience and Remote Sensing, 56(6), 3290-3299.

Arnell, N. W., and S. N. Gosling (2016), The impacts of climate change on river flood risk at the global scale, Climatic Change, 134(3), 387-401.

Bhatt, C. M., G. S., Rao, and S. Jangam (2020), Detection of urban flood inundation using RISAT-1 SAR images: a case study of Srinagar, Jammu and Kashmir (North India) floods of September 2014, Modeling Earth Systems and Environment, 6(1), 429-438.

Brisco, B., N. Short, J. v. d. Sanden, R. Landry, and D. Raymond (2009), A semi-automated tool for surface water mapping with RADARSAT-1, Canadian Journal of Remote Sensing, 35(4), 336-344.

Brisco, B., R. Touzi, J. J. van der Sanden, F. Charbonneau, T. Pultz, and M. D'Iorio (2008), Water resource applications with RADARSAT-2–a preview, International Journal of Digital Earth, 1(1), 130-147.

Brown, K. M., C. H. Hambidge, and J. M. Brownett (2016), Progress in operational flood mapping using satellite synthetic aperture radar (SAR) and airborne light detection and ranging (LiDAR) data, Progress in Physical Geography, 40(2), 196-214.

Chen, X.-L., H.-M. Zhao, P.-X. Li, and Z.-Y. Yin (2006), Remote sensing image-based analysis of the relationship between urban heat island and land use/cover changes, Remote sensing of environment, 104(2), 133-146.

Chini, M., R. Hostache, L. Giustarini, and P. Matgen (2017), A hierarchical split-based approach for parametric thresholding of SAR images: Flood inundation as a test case, IEEE Transactions on Geoscience and Remote Sensing, 55(12), 6975-6988.

Cohen, S., G. R. Brakenridge, A. Kettner, B. Bates, J. Nelson, R. McDonald, Y. F. Huang, D. Munasinghe, and J. Zhang (2018), Estimating floodwater depths from flood inundation maps and topography, JAWRA Journal of the American Water Resources Association, 54(4), 847-858.

Dasgupta, A., P. K. Thakur, and P. K. Gupta (2020), Potential of SAR-Derived Flood Maps for Hydrodynamic Model Calibration in Data Scarce Regions, Journal of Hydrologic Engineering, 25(9), 05020028.

Gan, T.Y., Zunic, F., Kuo, C.C. Strobl, T. (2012). Flood mapping of Danube river at Romania using single and multi-date ERS2SAR images. Int. J. Appl. Earth Obs. Geoinf., 18, 69-81

Gao, B.-C. (1996), NDWI—A normalized difference water index for remote sensing of vegetation liquid water from space, Remote sensing of environment, 58(3), 257-266.

Grimaldi, S., J. Xu, Y. Li, V. R. Pauwels and J. P. Walker (2020), Flood mapping under vegetation using single SAR acquisitions. Remote Sensing of Environment, 237, 111582.

Huang, M., and S. Jin (2020), Rapid flood mapping and evaluation with a supervised classifier and change detection in shouguang using sentinel-1 SAR and sentinel-2 optical data, Remote Sensing, 12(13), 2073.

Hultquist, C., and G. Cervone (2020), Integration of Crowdsourced Images, USGS Networks, Remote Sensing, and a Model to Assess Flood Depth during Hurricane Florence, Remote Sensing, 12(5), 834.

Jung, H. C., J. Hamski, M. Durand, D. Alsdorf, F. Hossain, H. Lee, A. A. Hossain, K. Hasan, A. S. Khan, and A. Z. Hoque (2010), Characterization of complex fluvial systems using remote sensing of spatial and temporal water level variations in the Amazon, Congo, and Brahmaputra Rivers, Earth Surface Processes and Landforms: The Journal of the British Geomorphological Research Group, 35(3), 294-304.

Jung, H. C., M. Jasinski, J. W. Kim, C. Shum, P. Bates, J. Neal, H. Lee, and D. Alsdorf (2012), Calibration of two-dimensional floodplain modeling in the central Atchafalaya Basin Floodway System using SAR interferometry, Water Resources Research, 48(7).

Kuenzer, C., H. Guo, J. Huth, P. Leinenkugel, X. Li, and S. Dech (2013), Flood mapping and flood dynamics of the Mekong Delta: ENVISAT-ASAR-WSM based time series analyses, Remote Sensing, 5(2), 687-715.

Kundzewicz, Z. W., S. Kanae, S. I. Seneviratne, J. Handmer, N. Nicholls, P. Peduzzi, R. Mechler, L. M. Bouwer, N. Arnell, and K. Mach (2014), Flood risk and climate change: global and regional perspectives, Hydrological Sciences Journal, 59(1), 1-28.

Lang, M. W., P. A. Townsend, and E. S. Kasischke (2008), Influence of incidence angle on detecting flooded forests using C-HH synthetic aperture radar data, Remote Sensing of Environment, 112(10), 3898-3907.

Li, Y., S. Martinis, M. Wieland, S. Schlaffer and R. Natsuaki (2019), Urban flood mapping using SAR intensity and interferometric coherence via Bayesian network fusion, Remote Sensing, 11(19), 2231.

Liang, J., and D. Liu (2020), Estimating daily inundation probability using remote sensing, riverine flood, and storm surge models: A case of hurricane Harvey, Remote Sensing, 12(9), 1495.

Lu, Z., and O.-i. Kwoun (2008), Radarsat-1 and ERS InSAR analysis over southeastern coastal Louisiana: Implications for mapping water-level changes

beneath swamp forests, IEEE Transactions on Geoscience and Remote Sensing, 46(8), 2167-2184.

Majidzadeh, H., H. Uzun, A. Ruecker, D. Miller, J. Vernon, H. Zhang, S. Bao, M. T. Tsui, T. Karanfil, and A. T. Chow (2017), Extreme flooding mobilized dissolved organic matter from coastal forested wetlands, Biogeochemistry, 136(3), 293-309.

Manjusree P, Kumar L.P., Bhatt C.M, Rao G.S, Bhanumurthy V. (2012). Optimization of threshold ranges for rapid flood inundation mapping by evaluating backscatter profiles of high incidence angle SAR images. International Journal of Disaster Risk Science. Jun 1;3(2):113-22.

Martinis, S., A. Twele, and S. Voigt (2009), Towards operational near real-time flood detection using a split-based automatic thresholding procedure on high resolution TerraSAR-X data, Natural Hazards & Earth System Sciences, 9(2) 303-314.

Martinis, S., and C. Rieke (2015), Backscatter analysis using multi-temporal and multi-frequency SAR data in the context of flood mapping at River Saale, Germany, Remote Sensing, 7(6), 7732-7752.

Min, S.-K., X. Zhang, F. W. Zwiers, and G. C. Hegerl (2011), Human contribution to more-intense precipitation extremes, Nature, 470(7334), 378-381.

O'Grady, D., M. Leblanc, and D. Gillieson (2013), Relationship of local incidence angle with satellite radar backscatter for different surface conditions, International journal of applied earth observation and geoinformation, 24, 42-53.

Pall, P., T. Aina, D. A. Stone, P. A. Stott, T. Nozawa, A. G. Hilberts, D. Lohmann, and M. R. Allen (2011), Anthropogenic greenhouse gas contribution to flood risk in England and Wales in autumn 2000, Nature, 470(7334), 382-385.

Plank, S., M. Jüssi, S. Martinis, and A. Twele (2017), Mapping of flooded vegetation by means of polarimetric Sentinel-1 and ALOS-2/PALSAR-2 imagery, International Journal of Remote Sensing, 38(13), 3831-3850.

Pradhan, B., M. I. Sameen, and B. Kalantar (2017), Optimized rule-based flood mapping technique using multitemporal RADARSAT-2 images in the tropical region, IEEE Journal of Selected Topics in Applied Earth Observations and Remote Sensing, 10(7), 3190-3199.

Psomiadis, E., K. X. Soulis, M. Zoka and N. Dercas (2019), Synergistic approach of remote sensing and GIS techniques for flash-flood monitoring and damage assessment in Thessaly Plain Area, Greece. Water, 11(3), 448.

Schlaffer, S., P. Matgen, M. Hollaus, and W. Wagner (2015), Flood detection from multi-temporal SAR data using harmonic analysis and change detection, International Journal of Applied Earth Observation and Geoinformation, 38, 15-24.

Scotti, V., M. Giannini and F. Cioffi (2020), Enhanced flood mapping using synthetic aperture radar (SAR) images, hydraulic modelling, and social media: A case study of Hurricane Harvey (Houston, TX), Journal of Flood Risk Management, 13(4), e12647.

Sharifi, A. (2020), Flood Mapping Using Relevance Vector Machine and SAR Data: A Case Study from Aqqala, Iran, Journal of the Indian Society of Remote Sensing, 48(9), 1289-1296.

Singh, A. (1989), 1989: Digital change detection techniques using remotely-sensed data. International Journal of Remote Sensing 10, 989-1003.

Smith, D. I. (1994), Flood damage estimation-A review of urban stage-damage curves and loss functions, Water Sa, 20(3), 231-238.

Twele, A., W. Cao, S. Plank, and S. Martinis (2016), Sentinel-1-based flood mapping: a fully automated processing chain, International Journal of Remote Sensing, 37(13), 2990-3004.

Van Westen, C. (2000), Remote sensing for natural disaster management, International archives of photogrammetry and remote sensing, 33(B7/4; PART 7), 1609-1617.

Voormansik, K., J. Praks, O. Antropov, J. Jagomägi, and K. Zalite (2013), Flood mapping with TerraSAR-X in forested regions in Estonia, IEEE Journal of Selected Topics in Applied Earth Observations and Remote Sensing, 7(2), 562-577.

Wan, L., M. Liu, F. Wang, T. Zhang and H. J. You (2019), Automatic extraction of flood inundation areas from SAR images: a case study of Jilin, China during the 2017 flood disaster. International journal of remote sensing, 40(13), 5050-5077.

Wdowinski, S., F. Amelung, F. Miralles-Wilhelm, T.H. Dixon, and R. Carande (2004), Space-based measurements of sheet-flow characteristics in the Everglades wetland, Florida, Geophysical Research Letters, 31(15).

Westra, S., L. V. Alexander, and F. W. Zwiers (2013), Global increasing trends in annual maximum daily precipitation, Journal of climate, 26(11), 3904-3918.

Woodhouse, I. H. (2017), Introduction to microwave remote sensing, CRC press.

Wu, C., X. Yang and J. Wang (2019), November, Flood Detection in Sar Images Based on Multi-Depth Flood Detection Convolutional Neural Network. In 2019 6th Asia-Pacific Conference on Synthetic Aperture Radar (APSAR) (pp. 1-6). IEEE.

Zeng, Z., Y. Gan, A. J. Kettner, Q. Yang, C. Zeng, G. R. Brakenridge and Y. Hong (2020), Towards high resolution flood monitoring: An integrated methodology using passive microwave brightness temperatures and Sentinel synthetic aperture radar imagery, Journal of Hydrology, 582, 124377.

Zhang, B., S. Wdowinski, T. Oliver-Cabrera, R. Koirala, M. Jo, and B. Osmanoglu (2018), Mapping the extent and magnitude of severe flooding induced by Hurricane IRMA with multi-temporal SENTINEL-1 SAR and Insar observations, Int. Arch. e Photogramm. Remote Sens. Spatial Inf. Sci, 42(43), 2237-2244.

Figure 1. The SAR image in the left plot shows the geographic extent of the study domain. The red boundary in the left plot indicates Pee Dee River basin and the shaded portion inside the basin boundary indicates the study area (aircraft flight domain). Hydrograph in the left plot shows the discharge at gauge B and red dots in it indicate the dates used in the analysis. The right plot displays a LiDAR-based DEM of the study area along with locations of USGS gauge points and approximate distance from the river mouth.

Gauge IDs: A=02110802; B=02135200; C=02131010; D=02131000; E=02130810; F=02130561; G=02130000 TA=02130980; and TB=02130930 (T=tributary)

Figure 2. Spatial plots of the estimated flood depth with LiDAR DEM and flood extent using Sentinel-1 and UAVSAR data

Figure3. A) Daily scatter plots showing the agreement between the estimated flood depth using LiDAR DEM and flood extent and the USGS gauge data. The Correlation coefficient R^2 between calculated and observed depth varies from 0.79 and 0.96 for the different dates and RMSE varies from 1.69 to 13.59 **B)** Scatter plots showing the change in water surface depth between September 18 and September 24, 2018 for the calculated using Sentinel-1 versus that observed using USGS gages. The correlation between the two is 0.9. **(C)** The (right) figure indicates change in water level between 18 and 24 September obtained from two different methods and their differences from the observed gauge data. The black column indicates difference in observed gauge data between two dates, light blue column indicates difference in depth obtained from DEM, and dark blue column indicates difference obtained from InSAR.

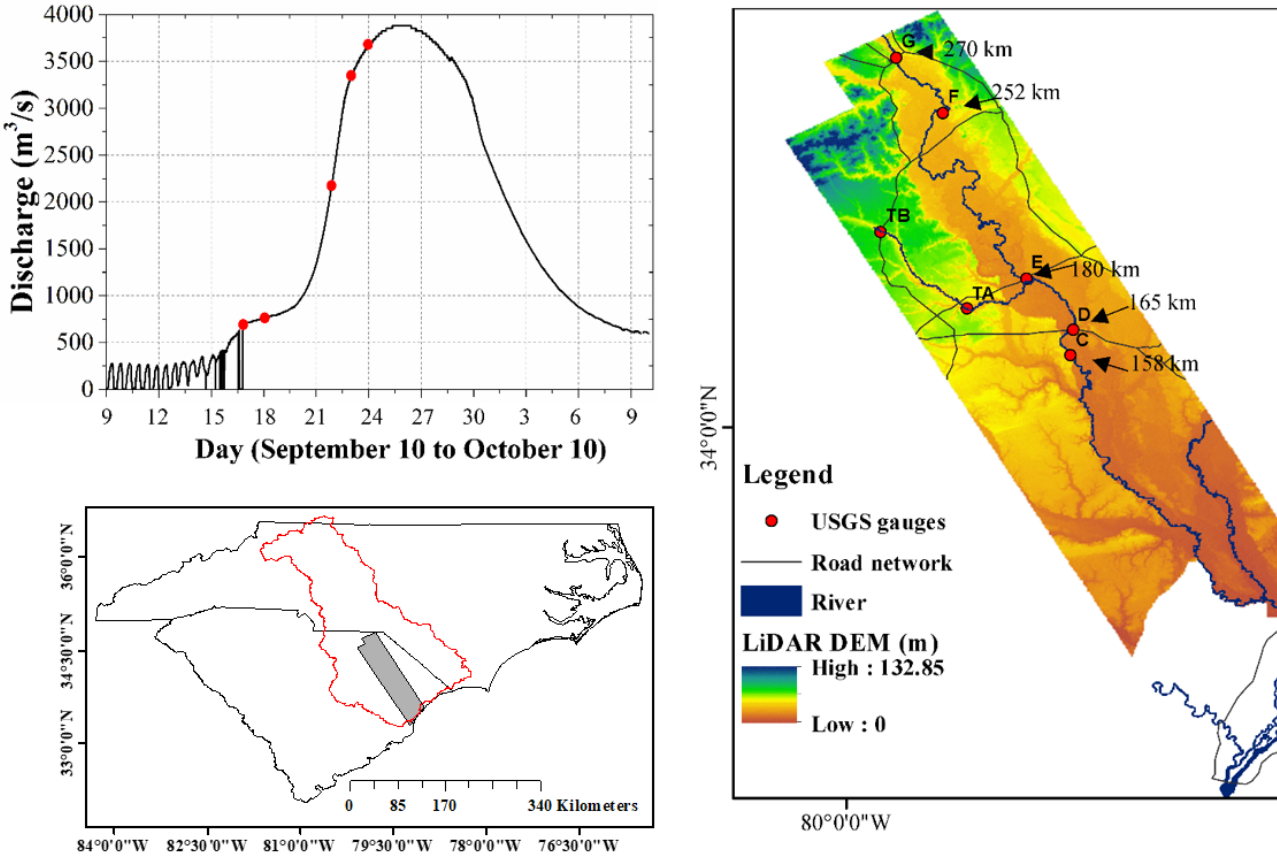

Figure 1 The SAR image in the left plot shows the geographic extent of the study domain. The red boundary in the left plot indicates Pee Dee River basin and the shaded portion inside the basin boundary indicates the study area (aircraft flight domain). Hydrograph in the left plot shows the discharge at gauge B and red dots in it indicate the dates used in the analysis. The right plot displays a LiDAR-based DEM of the study area along with locations of USGS gauge points and approximate distance from the river mouth.

Gauge IDs: A=02110802; B=02135200; C=02131010; D=02131000; E=02130810; F=02130561; G=02130000 TA=02130980; and TB=02130930 (T=tributary)

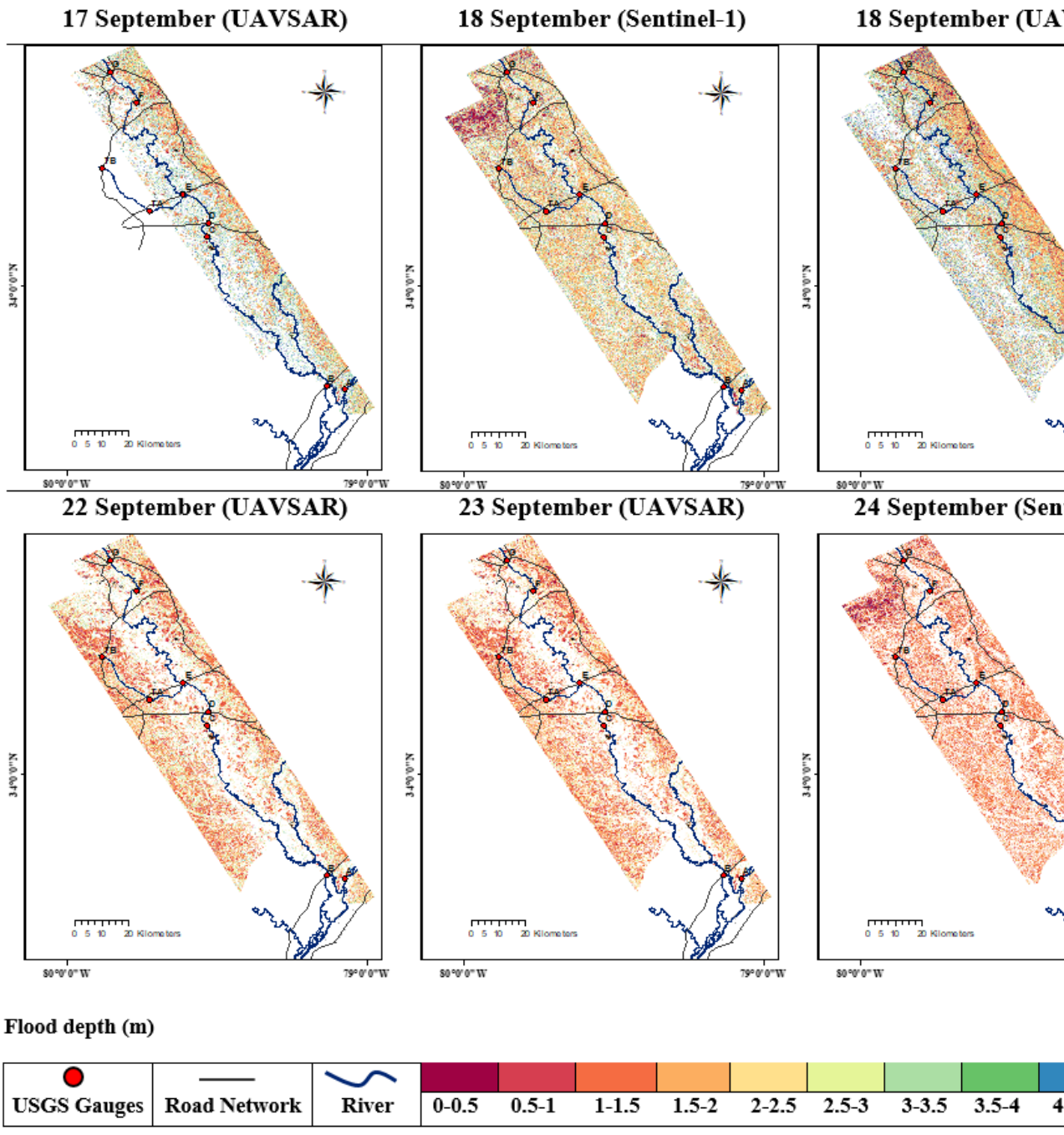

Figure 2 Spatial plots of the estimated flood depth with LiDAR DEM and flood extent using Sentinel-1 and UAVSAR data.

(A)

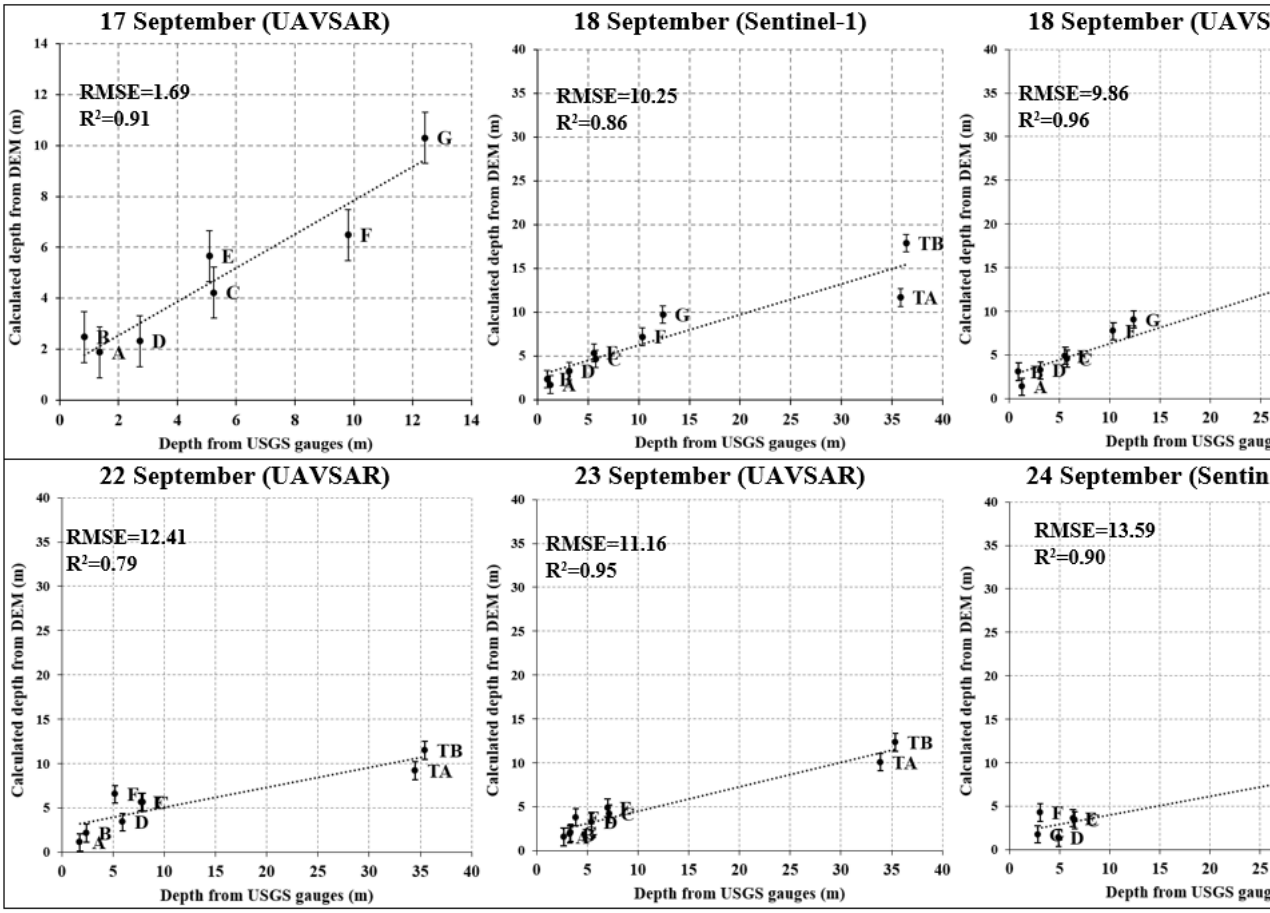
17 September (UAVSAR)
RMSE=1.69
R²=0.91
18 September (Sentinel-1)
RMSE=10.25
R²=0.86
18 September (UAVS
RMSE=9.86
R²=0.96
22 September (UAVSAR)
RMSE=12.41
R²=0.79
23 September (UAVSAR)
RMSE=11.16
R²=0.95
24 September (Sentin
RMSE=13.59
R²=0.90
Calculated depth from DEM (m)
Depth from USGS gauges (m)
A
B
C
D
E
F
G
TA
TB

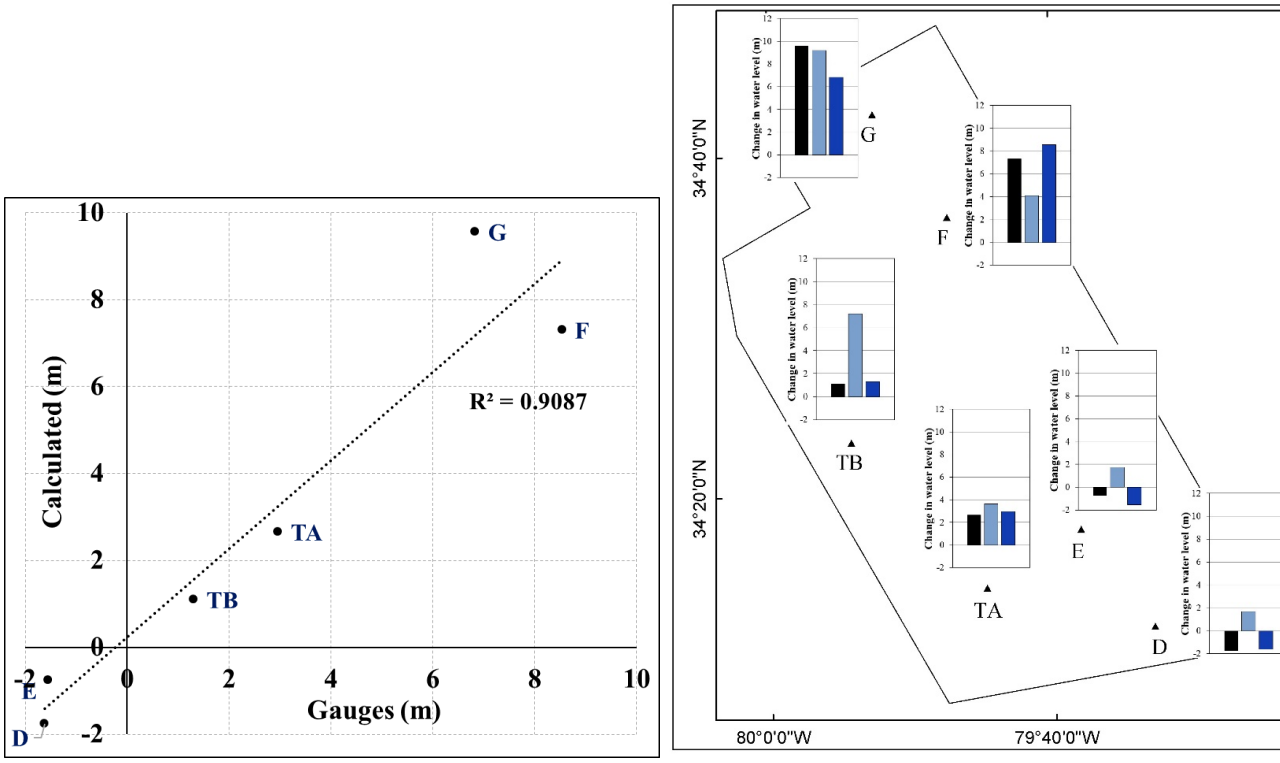

Figure 3. A) Daily scatter plots showing the agreement between the estimated flood depth using LiDAR DEM and flood extent and the USGS gauge data. The Correlation coefficient R^2 between calculated and observed depth varies from 0.79 and 0.96 for the different dates and RMSE varies from 1.69 to 13.59 B) Scatter plots showing the change in water surface depth between September 18 and September 24, 2018 for the calculated using Sentinel-1 versus that observed using USGS gages. The correlation between the two is 0.9. (C) The (right) figure indicates change in water level between 18 and 24 September obtained from two different methods and their differences from the observed gauge data. The black column indicates difference in observed gauge data between two dates, light blue column indicates difference in depth obtained from DEM, and dark blue column indicates difference obtained from InSAR.